Independent confirmation of a methane spike on Mars and a source region east of Gale Crater

Authors: Marco Giuranna[1]*, Sébastien Viscardy[2], Frank Daerden[2], Lori Neary[2], Giuseppe Etiope[3,1], Dorothy Oehler[4], Vittorio Formisano[†], Alessandro Aronica[1], Paulina Wolkenberg[1,5], Shohei Aoki[1,2,6,7], Alejandro Cardesín-Moinelo[8], Julia Marín-Yaseli de la Parra[8], Donald Merritt[8], Marilena Amoroso[9]

Affiliations:

[1]Istituto di Astrofisica e Planetologia Spaziali (INAF-IAPS), Via del Fosso del Cavaliere 100, 00133 Rome, Italy.

[2]Royal Belgian Institute for Space Aeronomy, Avenue Circulaire 3, 1180 Brussels, Belgium

[3]Istituto Nazionale di Geofisica e Vulcanologia, via V. Murata 605, 00143 Rome, Italy, and Faculty of Environmental Science and Engineering, Babes-Bolyai University, Cluj-Napoca, Romania

[4]Planetary Science Institute, 1700 East Fort Lowell Road, Tucson, Arizona 85719 USA

[5]Centrum Badan Kosmicznych Polska Akademia Nauk, ul. Bartycka 18a, Warsaw, Poland

[6]Fonds National de la Recherche Scientifique, rue d'Egmont 5, B-1000 Brussels, Belgium

[7]Department of Geophysics, Tohoku University, Sendai, Miyagi 980-8578, Japan.

[8]European Space Astronomy Centre, Villanueva de la Cañada, E-28692, Madrid, Spain

[9]Agenzia Spaziale Italiana, Sede di Matera, Italy

*Correspondence to: marco.giuranna@iaps.inaf.it

[†] This paper is dedicated to the memory of our wonderful colleague, Dr. Vittorio Formisano, former PI for PFS-Mex, who recently passed away.

Reports of methane detection in the Martian atmosphere have been intensely debated. The presence of methane could enhance habitability and may even be a signature of life. However, no detection has been confirmed with independent measurements. Here we report a firm detection of 15.5 ± 2.5 parts per billion by volume of methane in the Martian atmosphere above Gale crater on 16 June 2013, by the Planetary Fourier Spectrometer onboard Mars Express, one day after the in-situ observation of a methane spike by the Curiosity Rover. Methane was not detected in other orbital passages. The detection uses improved observational geometry as well as more sophisticated data treatment and analysis, and constitutes a contemporaneous, independent detection of methane. We perform ensemble simulations of the Martian atmosphere, using stochastic gas release scenarios to identify a potential source region east of Gale crater. Our independent geological analysis also points to a source in this region, where faults of Aeolis Mensae may extend into proposed shallow ice of the Medusae Fossae Formation and episodically release gas trapped below or within the ice. Our identification of a likely release location will provide focus for future investigations into the origin of methane on Mars.

Since its discovery in the Martian atmosphere[1–4], there has been a continuing debate about the origin of methane (CH_4), and several generation mechanisms, both abiotic and biotic, have been proposed[5–17]. Despite various detections reported by separate groups and different experiments, the methane debate still splits the Mars community. Although plausible mechanisms have been proposed to explain the observed abundance, variability, and lifetime of methane in the current Martian atmosphere[18–34], doubts about its very existence still arise. Previous detections have been considered tentative[35] due to either the challenge of discriminating telluric and Martian features when observing from Earth (claims later rebutted[23]) or the limited spectral resolving power and/or signal-to-noise ratio of space-borne observations[18-20]. In-situ detection of CH_4 at Gale crater[4] by the Tunable Laser Spectrometer-Sample Analysis at Mars (TLS-SAM) on Curiosity has also been questioned[36] as potentially coming from the rover itself, although that possibility was ruled out by the Curiosity team[24]. However, while several non-detections have been reported, none of the positive detections have been confirmed so far with independent measurements.

Methane detection by the Planetary Fourier Spectrometer (PFS)

The Mars Express (MEx) spacecraft[37] was designed to operate in several science pointing modes, including nadir pointing and spot pointing. Most PFS[38] observations are acquired in nadir pointing[2,18,19]. The spot-tracking mode, which points the optical instruments to a surface feature on Mars and tracks it, was exploited in this study for the first time. These observations are particularly suitable for methane retrievals because they allow acquisition of several hundred spectra over one area in a relatively short time (typically a few tens of minutes). The ensemble average of these measurements enhances the statistical importance of the PFS observations, as detailed in the Supplementary Information (noted hereafter SI). In Supplementary **Table S1,** we summarize the list of spot-tracking observations over Gale crater performed by the PFS from December 2012 to July 2014, which roughly corresponds to the first 20-month period of methane measurements at Gale crater by Curiosity's TLS-SAM[4].

PFS observed elevated levels of methane of 15.5 ± 2.5 ppbv, column-integrated abundance, in orbit 12025, on June 16, 2013 (**Table 1**). This date just follows Martian solar day (*sol*) 305 after the landing of the Curiosity rover[24], when the TLS-SAM also reported a methane spike of 5.78 ± 2.27 ppbv. Our results, therefore, provide the first contemporaneous detection of methane in the Martian atmosphere by *in situ* and remote sensing measurements. In **Fig. 1a,** we show the PFS average spectrum for orbit 12025 (280 measurements collected in about 45 minutes in spot-tracking mode) compared to synthetic best-fit spectra. In **Fig. 1b** we subtract the synthetic best-fit spectrum with no methane to the PFS spectrum. The CH_4 absorption band observed by PFS becomes evident in the differential spectrum (**Fig. 1b**). The relatively high spectral resolution and the new data handling allow unambiguous identification of the CH_4 Q-branch at 3018 cm^{-1} by the PFS near-infrared spectra. Considering the 1-σ uncertainty, methane abundances ranging from 13 to 18 ppbv are consistent with the observed intensity of the CH_4 absorption band. A detailed description of the new PFS data treatment and of the improved characterization of the PFS apodized instrument line shape is reported in in SI-1. The algorithm adopted for the CH_4 retrievals is described in the Methods section.

In the almost two-year period of spot-tracking observations reported here (22 in total), there was no other occasion on which PFS made a positive detection of methane over Gale crater (see **Table S1**). PFS did not perform any spot-tracking observation during the second TLS-SAM high-methane period (sol 466 to sol 526), but there are 10 spot-tracking observations in the later period when no methane was detected, with a detection limit of 2-4 ppbv. This is consistent with the low methane measurements by TLS-SAM in the same period. In addition, no evidence of methane was found in 3 nadir observations performed a few days apart from sol 306 in the area surrounding Gale crater (**Table 1 and Fig. S12a**). An example of non-detection is shown in **Fig. S12b** for MEx orbit 12018 (one sol before the TLS-SAM spike detection on sol 305, **Table 1**). An upper-limit of 3 ppbv of CH_4 is retrieved from the average of 276 PFS measurements collected in this orbit.

The search for CH_4 source regions

The contemporaneous detection of methane provides unique information to use in search for its source locations. The available data in a 14-sol time window (Sols 304 – 318; **Table 1**) provide evidence that the sol 305-306 observations by the PFS and the TLS-SAM sampled the same methane release event, and that this event is limited in time. Although several production mechanisms and sources of methane have been discussed in the literature[6–17], terrestrial analogues argue that subsurface accumulations are the most likely sources (see SI-2). Subsurface methane could have been produced by either abiotic or biotic processes and stored in clathrates, zeolites, or reservoir rocks (any permeable or fractured rock) sealed by permafrost or other impermeable rocks before being outgassed through fractures and faults[16]. Accordingly, in this paper, we focus on the hypothesis of surface release. Exogenous processes that may add methane to the Martian atmosphere[17] are not considered in this work.

It was argued that a gas emission possibly explaining the detection by TLS-SAM on sol 305 was most likely weak and local (possibly inside the crater) and took place to the north of Curiosity because the prevailing daytime near-surface winds are southwards[4]. However, the vertically-integrated methane abundance measured by PFS one sol later changes our understanding of the release event. The amount of methane measured by PFS corresponds to ~39-54 tonnes that were present in the area of ~49,000 km^2 observed from orbit (**Fig. 2**). The combination of PFS and TLS observations strongly suggest that the emission took place outside the crater (see SI-3), making a general circulation model (GCM) an appropriate choice for a first interpretation of these observations. To simulate methane transport, we applied the three-dimensional GEM-Mars model[28,40,41] (see Methods). Wind fields simulated in the GCM show a variability with local time and with height (see **Fig. S17**), increasing the complexity of methane transport compared to previous assumptions[4].

The search for the source of methane based on a few observations is an under-constrained problem. The constraints provided by the available observations (**Table 1**) suggest that the release event was relatively short and occurred not very far from the crater. Methane released from a localized source would rapidly disperse[28] whereas a distant source would require very large amounts of methane to be emitted, which is inconsistent with the observations. Preliminary model tests led to the following assumptions that restrict the problem: (i) the source is unlikely to be more distant than ~800 km from the crater, and (ii) the emission did not start prior to sol 302. We considered 30 model grid cells within a 24°×20° area centered at Gale as potential emission sites (**Fig. 2**). The problem remains weakly constrained as no direct information is available on the source's location, and the initial time, duration, temporal variations and strengths of gas fluxes characterizing the release pattern. For this reason, we developed an *ensemble approach* considering a very large sample of possible emission scenarios in order to identify the most likely sources *in terms of probability.*

We considered methane emission patterns (release intensity, duration, temporal variation) that are based on gas seepage theory and consistent with methane seepage phenomena observed on Earth[42] (see SI-2 for details). We assumed an "episodic" seepage scenario for the methane release (**Fig. S7**), which is most consistent with previous detections[1–4]. An episodic emission may be characterized by one single major pulse or a series of short-term seepage oscillations (SI-2). From each of the 30 possible emission sites considered in the model, a series of 30-minute-long methane pulses was applied for a total duration of 5 sols (from sol 302 to 307). Exploiting the linear additivity of the methane tracers (as the methane is chemically inert on the considered timescale, and the feedback of methane on the atmospheric dynamics is negligible), the tracers were linearly combined by random numbers to produce release scenarios composed of stochastic fluxes. A total of 10^6 different combinations was generated for each of the 30 considered release sites. For these patterns, the initial times and durations of emission were also generated randomly. As a result, the constructed episodic emission scenarios last from 30 minutes to 5 sols. The large number (10^6) of emission scenarios considered in each of the model grid cells forms a statistically representative sample of all possible release scenarios from a specific site **(Fig. S16)**.

The simulated scenarios were then compared with the observational constraints in **Table 1**. The number of scenarios consistent with the observations divided by the sample size then gives the probability that a methane release from a given emission site fits the observations (see Methods). The result is shown in a *probability map* (**Fig. 3)**. Sites to the north, west and south-west of Gale have no significant probability for being source locations. The sites to the east and south-east of Gale crater yield the highest probabilities as source locations, especially Blocks E8 and ESE with probabilities of 42.4% and 54.0%, respectively, meaning that about half of all the generated emission patterns released from these sites can reproduce the entire set of observations in **Table 1**. The total mass of methane released from E8 (ESE) in 95% of scenarios fitting the observations is 1,170 – 2,740 tonnes (1,590 – 4,050 tonnes), which corresponds to an enhancement of ~0.1 – 0.3 ppbv (0.2 – 0.4 ppbv) to the global mean mixing ratio, after the gas is well-mixed around the planet. These abundances can be considered as upper limits for the mass released, given the coarse resolution of the GCM.

Geological context

We investigated the Martian geological context in search of structures that might be associated with methane release (e.g., faults, hydrothermal-volcanic vents, springs, and mud volcanoes[16]), applying knowledge of relationships between gas seepage and tectonic/morphological structures, as observed on Earth[42]. Gas seepage occurs along faults, of any type, regardless the tectonic conditions. Details of terrestrial gas seepage and geological assessment of the Martian area of interest determined from atmospheric modelling (**Fig. 2**) are provided in SI-2. Conclusions about relative merits of different grid blocks were reached independently from the GCM analysis, by a separate team.

Potential methane release structures were identified along the eastern side of the grid, in Block E8 and subordinately in Blocks ENE, E12, ESE, and ESEE (**Fig. 4**). Block E8 includes the Noachian-Hesperian fretted terrain of Aeolis Mensae[43] in contact with the younger, Hesperian-Amazonian, Medusae Fossae Formation (MFF) and in close proximity to locations where the MFF has been proposed to contain shallow bulk ice (from water-equivalent-hydrogen > ~26%[44]). Since permafrost is one of the best seals for methane[16], it is possible that bulk ice in the MFF may trap and seal subsurface methane. That methane could be released episodically along faults that break through the permafrost due to partial melting of ice, gas pressure build-up induced by gas accumulation during migration, or stresses due to planetary adjustments or local meteorite impact[16] (see also SI-2). The distribution of geological outcrops suggests that Aeolis Mensae deposits underlie the area of bulk ice (**Fig. 4**). Faults of Aeolis Mensae, being associated with the Martian dichotomy, may be deeply rooted[16] (SI-2) and may have provided long-lived conduits for migrating methane and liquid water, the latter perhaps contributing to accumulation of shallow ice in the MFF. In addition, the many fault intersections of Aeolis Mensae may enhance permeability and thus degassing, as on Earth[42]. Several lineations appear to offset dunes and yardangs in the MFF of Block E8 (**Fig. S8)** and may be relatively recent. These lineations have orientations similar to faults of Aeolis Mensae and may be surface expressions of reactivated Aeolis Mensae/dichotomy faults at depth, providing pathways for gas seepage through an otherwise sealing permafrost.

Blocks ESE and ESEE contain extensions of Aeolis-Mensae dichotomy faults in their north-eastern and northern portions, respectively. Block ESE is farther from the bulk ice (**Fig. 4**) than Block E8, and Block ESEE is still farther. Block ESE however contains unusual flow-like structures (**Fig. S8**), and work is continuing to assess whether these might be methane-release structures. Other blocks are of lesser merit (see SI-2).

Thus, the eastern sector of the grid contains features that could trap subsurface methane and account for its present-day, episodic release. Of these, Block E8 is the highest ranked, as it has potentially recent faults closest to the proposed ice. Because the area affected by faults and ice is large (10^2-10^4 km^2; **Fig. 4**), methane flux from either diffuse microseepage or seeps along faults in the ice could account for the methane detected by the PFS (see SI-2 and **Fig. S10**).

A first step to understanding the origin of methane on Mars

This work presents the first independent confirmation of methane detection on Mars and the first synergistic approach to the search for potential sites of methane release, integrating orbital and ground-based detections with Martian geology and atmospheric simulations (using gas emission scenarios based on terrestrial seepage data). This approach provides a template for future efforts aimed at locating sites on Mars of methane release from the subsurface. While this work relies on the hypothesis of a surface release, other explanations remain possible, but given a surface release, our work provides the first constraints for source locations.

The results of the GCM and geological analyses are remarkable, as each line of investigation independently pointed to the same area east/southeast of Gale as the most likely source location for the methane (**Figs. 3-4**). Block E8 is singled out, as it contains multiple faults and fault intersections of Aeolis Mensae along with possible extensions of those faults into proposed shallow ice in the overlying MFF. Such ice could have sealed subsurface methane and recent reactivation of Aeolis Mensae/dichotomy faults could have penetrated the ice, episodically opening enhanced release pathways.

The results presented in this work not only corroborate previous detections by Curiosity but, in a broader perspective, might change our view of methane occurrence on Mars. Rather than by large emissions and a global presence, our data suggest that the presence of methane on Mars might be characterized by small, short emissions and transient events. This possibility has been raised before[35,42], but further investigations are required to understand processes of rapid methane loss and reconcile these new PFS findings with the anticipated TGO results[47].

We do not address the ultimate origin of the detected Martian methane. Many abiotic and biotic processes can generate methane on Mars[6–17]. However, the first step to understanding the origin of any Martian methane is to determine its release location. From there, detailed follow-up should eventually reveal the mode of generation and significance of detected methane[48]. The PFS instrument will continue its monitoring of the Martian atmosphere. The new approach, described here, to PFS data selection, processing and retrieval will also be applied to the entire PFS dataset for a complete re-analysis. In addition, spot-tracking observations will be performed over geologically-determined potential source regions of methane, including the region identified in this work, providing a test of the model of subsurface release. The ExoMars Trace Gas Orbiter payload[49,50] will also continue its search for methane from Mars orbit, and coordinated observations with PFS are being planned.

References

1. Krasnopolsky, V. A., Maillard, J. P. & Owen, T. C., Detection of methane in the Martian atmosphere: Evidence for life? *Icarus* **172**, 537–547 (2004). doi:10.1016/j.icarus.2004.07.004
2. Formisano, V., Atreya, S., Encrenaz, T., Ignatiev, N. & Giuranna, M., Detection of methane in the atmosphere of Mars. *Science* **306**, 1758–1761 (2004). doi:10.1126/science.1101732
3. Mumma, M. J., et al., Strong release of methane on Mars in northern summer 2003. *Science* **323**, 1041–1045 (2009). doi:10.1126/science.1165243
4. Webster, C. R. et al., Mars methane detection and variability at Gale crater. *Science* **347**, 415–417 (2015). doi:10.1126/science.1261713
5. Yung, Y. et al., Methane on Mars and habitability: Challenges and Responses. *Astrobiology* **18** (10), 1221–1242 (2018). doi:10.1089/ast.2018.1917
6. Atreya, S. K., Mahaffy, P. R. & Wong, A. S., Methane and related trace species on Mars: Origin, loss, implications for life, and habitability. *Planet. Space Sci.* **55**, 358–369 (2007). doi:10.1016/j.pss.2006.02.005
7. Oze, C. & Sharma, M., Have olivine, will gas: Serpentinization and the abiogenetic production of methane on Mars. *Geophys. Res. Lett.* **32**, L10203 (2005). doi:10.1029/2005GL022691
8. Krasnopolsky, V. A., Some problems related to the origin of methane on Mars. *Icarus* **180**, 359–367 (2006). doi:10.1016/j.icarus.2005.10.015
9. Chassefière, E., Metastable methane clathrate particles as a source of methane to the Martian atmosphere. *Icarus* **204**, 137–144 (2009). doi:10.1016/j.icarus.2009.06.016
10. Gough, R. V., Tolbert, M. A., McKay, C. P. & Toon, O. B., Methane adsorption on a Martian soil analog: An abiogenic explanation for methane variability in the Martian atmosphere. *Icarus* **207**, 165–174 (2010). doi:10.1016/j.icarus.2009.11.030

11. Meslin, P.-Y., Gough, R., Lèfevre, L. & Forget, F., Little variability of methane on Mars induced by adsorption in the regolith. *Planet. Space Sci.* **59**, 247–258 (2011). doi:10.1016/j.pss.2010.09.022

12. Keppler, F., et al., Ultraviolet-radiation-induced methane emissions from meteorites and the Martian atmosphere. *Nature* **486**, 93–96 (2012). doi:10.1038/nature11203

13. Schuerger, A., Moores, J. E., Clausen, C. A., Barlow, N. G. & Britt, D. T., Methane from UV-irradiated carbonaceous chondrites under simulated Martian conditions. *J. Geophys. Res.* **117**, E08007 (2012). doi:10.1029/2011JE004023

14. McMahon, S., Parnell, J. & Blamey, N. J. F., Sampling methane in basalt on Earth and Mars. *Int. J. Astrobiol.* **12**, 113–122 (2013). doi:10.1017/S1473550412000481

15. Poch, O., Kaci, S., Stalport, F., Szopa, C. & Coll, P., Laboratory insights into the chemical and kinetic evolution of several organic molecules under simulated Mars surface UV radiation conditions. *Icarus* **242**, 50–63 (2014). doi:10.1016/j.icarus.2014.07.014

16. Oehler, D. & Etiope, G., Methane seepage on Mars: where to look and why. *Astrobiology* **17**, 1233–1264 (2017). doi:10.1089/ast.2017.1657

17. Fries, M., et al., A cometary origin for martian atmospheric methane. *Geochem. Persp. Let.* **2**, 10–23 (2016). doi:10.7185/geochemlet.1602

18. Geminale, A., Formisano, V. and Giuranna, M., Methane in Martian atmosphere: Average spatial, diurnal, and seasonal behavior. *Planet. Space Sci.* **56**, 1194–2003 (2008). doi:10.1016/j.pss.2008.03.004

19. Geminale, A., Formisano, V. & Sindoni, G., Mapping methane in Martian atmosphere with PFS-MEx data. *Planet. Space Sci.* **59**, 137–148 (2011). doi:10.1016/j.pss.2010.07.011

20. Fonti, S. & Marzo, G. A., Mapping the methane on Mars. *Astron. Astrophys.* **512**, A51 (2010). doi:10.1051/0004-6361/200913178

21. Krasnopolsky, V. A., A sensitive search for methane and ethane on Mars, *EPSC abstracts* **6**, 49 (2011).

22. Krasnopolsky, V. A., Search for methane and upper limits to ethane and SO_2 on Mars. *Icarus* **217**, 144–152 (2012). doi:10.1016/j.icarus.2011.10.019

23. Villanueva, G. L., et al., A sensitive search for organics (CH_4, CH_3OH, H_2CO, C_2H_6, C_2H_2, C_2H_4), hydroperoxyl (HO_2), nitrogen compounds (N_2O, NH_3, HCN) and chlorine species (HCl, CH_3Cl) on Mars using ground-based high-resolution infrared spectroscopy. *Icarus* **223**, 11–27 (2013). doi:10.1016/j.icarus.2012.11.013

24. Webster, C. R. et al., Background levels of methane in Mars' atmosphere show strong seasonal variations, *Science* **360**, 6393, 1093-1096 (2018), doi:10.1126/science.aaq0131

25. Summers, M. E., Lieb, B. J., Chapman, E. & Yung, Y. L., Atmospheric biomarkers of subsurface life on Mars, *Geophys. Res. Lett.* **29**(24), 2171 (2002). doi:10.1029/. 2002GL015377

26. Lefèvre, F. & Forget, F., Observed variations of methane on Mars unexplained by known atmospheric chemistry and physics. *Nature* **460**, 720–723 (2009). doi:10.1038/nature08228

27. Atreya, S. K., et al., Methane on Mars: Current observations, interpretations, and future plans. *Planet. Space Sci.* **59**, 133–136 (2011). doi:10.1016/j.pss.2010.10.008

28. Viscardy, S., Daerden, F. & Neary, L., Formation of layers of methane in the atmosphere of Mars after surface release, *Geophys. Rev. Lett.* **43**, 1868–1875 (2016). doi:10.1002/2015GL067443

29. Holmes, J. A., Patel, M. R. & Lewis, S. R., The vertical transport of methane from different potential emission types on Mars, *Geophys. Res. Lett.* **44**, 8611–8620 (2017). doi:10.1002/2017GL074613

30. Holmes, J. A., Lewis, S. R. & Patel, M.R., Analyzing the consistency of Martian methane observations by investigation of global methane transport. *Icarus* **257**, 23–32 (2015). doi:10.1016/j.icarus.2015.04.027

31. Farrell, W. M., Delory, G. T. & Atreya, S. K., Martian dust storms as a possible sink of atmospheric methane. *J. Geophys. Res.* **33**, L21203 (2006). doi:10.1029/2006GL027210

32. Atreya, S. K., et al., Oxidant enhancement in Martian dust devils and storms: Implications for life and habitability. *Astrobiology* **6**, 439–450 (2006). doi:10.1089/ast.2006.6.439

33. Delory, G. T., et al., Oxidant enhancement in Martian dust devils and storms: Storm electric fields and electron dissociative attachment. *Astrobiology* **6**, 451–462 (2006). doi:10.1089/ast.2006.6.451

34. Jensen, S. K. et al., A sink for methane on Mars? The answer is blowing in the wind. *Icarus* **236**, 24–27 (2014). doi:10.1016/j.icarus.2014.03.036

35. Zahnle, K. J., Freedman, R. S. & Catling, D. C., Is there methane on Mars? *Icarus* **212**, 493–503 (2011). doi:10.1016/j.icarus.2010.11.027

36. Zahnle, K. J., Play it again, SAM. *Science* **347**, 370-371 (2015). doi:10.1126/science.aaa3687

37. Wilson, A. & Chicarro, A., *Mars Express: the Scientific Payload*. Ed. by Andrew Wilson, scientific coordination: Agustin Chicarro. ESA SP-1240, Noordwijk, Netherlands: ESA Publications Division, ISBN 92-9092-556-6, XIV + 216 pp. (2004).

38. Formisano, V., et al., The Planetary Fourier Spectrometer (PFS) onboard the European Mars Express mission. Planet. Space Sci. 53 (10), 963-974 (2005). doi:10.1016/j.pss.2004.12.006

39. Knapmeyer, M., et al., Working models for spatial distribution and level of Mars' seismicity. *J Geophys Res* **111**, E11006 (2006). doi:10.1029/2006JE002708

40. Neary, L. & Daerden, F., The GEM-Mars general circulation model for Mars: Description and evaluation. *Icarus* **300**, 458–476 (2018). doi:10.1016/j.icarus.2017.09.028

41. Daerden, F., et al., A solar escalator on Mars: Self-lifting of dust layers by radiative heating. *Geophys. Res. Lett.* **42**, 7319–7326 (2015). doi:10.1002/2015GL064892

42. Etiope, G. & Oehler, D.Z., Methane spikes, background seasonality and non-detections on Mars: a geological perspective. *Planet. Space Sci*., in press (2019).

43. Kerber, L. & Head, J. W., The age of the Medusae Fossae Formation: Evidence of Hesperian emplacement from crater morphology, stratigraphy, and ancient lava contacts. *Icarus* **206**, 669-684 (2010). doi:10.1016/j.icarus.2009.10.001

44. Wilson, J. T., et al., Equatorial locations of water on Mars: Improved resolution maps based on Mars Odyssey Neutron Spectrometer data. *Icarus* **299**, 148–160 (2018). doi:10.1016/j.icarus.2017.07.028

45. Lanz, J. K. & M. B. Saric, Cone fields in SW Elysium Planitia: Hydrothermal venting on Mars. *J. Geophys. Res.* **114**, E02008 (2009). doi:10.1029/2008JE003209.

46. Martínez-Alonso, S., Mellon, M. T., McEwen, A. S. & the HiRISE Team, Geological study of a section of Aeolis Mensae, a possible site favorable for life. 7th International conference on Mars, Abs. No. 3262 (2007).

47. Voosen, P., Martian methane - spotted in 2004 - has mysteriously vanished, *Science* (2018). doi:10.1126/science.aaw3667

48. Etiope G., Understanding the origin of methane on Mars through isotopic and molecular data from the ExoMars orbiter. *Planet. Space Sci.* **159**, 93–96 (2018). doi:10.1016/j.pss.2018.04.020

49. Vandaele, A. C. et al., NOMAD, an Integrated Suite of Three Spectrometers for the ExoMars Trace Gas Mission: Technical Description, Science Objectives and Expected Performance. *Space Sci. Rev.* **214**, 80 (2018). doi:10.1007/s11214-018-0517-2

50. Korablev, O. et al., The Atmospheric Chemistry Suite (ACS) of Three Spectrometers for the ExoMars 2016 Trace Gas Orbiter. Space Sci. Rev. **214**, 7 (2018). doi:10.1007/s11214-017-0437-6

Acknowledgements

We thank Environment and Climate Change Canada for providing the GEM model for research purposes and for their support. We thank Jack T. Wilson for providing data used to map the water-equivalent-hydrogen from improved resolution Mars Odyssey Neutron Spectrometer data. We thank the efforts of O. Witasse, D. Titov, P. Martin, and the ESA Science Ground Segment and Flight Control Teams for the successful operations of the Mars Express mission over more than a decade. The PFS experiment has been built at the Institute for Space Astrophysics and Planetology (IAPS) (former IFSI, Institute for Interplanetary Space Physics) of the National Institute for Astrophysics (INAF) and is currently funded by the Italian Space Agency (ASI, agreement n. 2018-2-HH.0) in the context of the science activities for NOMAD/ACS-TGO Exomars 2016 and PFS/Mars Express. DZO is supported by the Planetary Science Institute. SV and LN are supported by the ESA PRODEX Office, contract no. Prodex_NOMADMarsScience_C4000121493_2017-2019. SV is also supported by the "Excellence of Science" project "Evolution and Tracers of Habitability on Mars and the Earth" (FNRS 30442502). PW is supported by the UPWARDS project, funded from the European Union's Horizon 2020 research and innovation programme under grant agreement No. 633127. SA has been supported by the FNRS "CRAMIC" project under grant agreement n◦ T.0171.16.

Author Contributions

M.G. and S.A. developed the new approach to PFS data selection and treatment. M.G. performed the CH_4 retrieval. A.A., P.W. and S.A. supervised the PFS science operations, planning, commanding, and data archiving. A.C.-M. provided ancillary data and other geometrically relevant models for PFS and MEx through the SPICE software suite. A.C.-M., J.M.-Y.P. and D.M. contributed to the planning of PFS observations and to the successful implementation and execution of PFS spot-tracking observations. V.F. developed the concept and was the former PI for PFS-MEx. S.V., F.D. and L.N. developed and performed the GCM simulations and analysis. G.E. and D.O. performed the geological analysis and the evaluation of terrestrial seepage patterns. M.A. were responsible for the PFS-MEx project from the Italian Space Agency side. All authors contributed to interpretation of the results and the preparation of the manuscript.

Competing interests

The authors declare no competing interests.

Figure captions

Fig. 1 | PFS retrieval of CH_4 abundance from orbit 12025. a, Synthetic best-fit spectra (black curves) are compared to the PFS average spectrum (red). H_2O abundance is 350 ppm in all spectra. Water vapor and solar lines are also indicated. **b**, The best-fit synthetic spectrum with 0 ppbv of methane shown in **a** is subtracted from the PFS average spectrum (black) and from the synthetic spectra with 13 and 18 ppbv of methane (red and blue curve, respectively). The orange line marks the zero level. 1-σ error-bars are shown in (a) and (b) (see SI-1 for details).

Fig. 2 | Location map and regional setting. Basemap, MOLA elevation on MOLA Hillshade. White grid is area of interest from atmospheric modelling. Red lines, extensional faults; blue lines, compressional faults[39]. Black outline around Gale crater is the envelope of PFS footprints for orbit 12025. Yellow triangle, location of the Curiosity rover.

Fig. 3 | Probabilities estimated for the 30 emission sites. The probability is defined as the number of release scenarios consistent with the observations divided by the sample size. Basemap as in **Fig. 2**.

Fig. 4 | Geological context of grid blocks. MFF, Medusae Fossae Formation. Black dots, sites with Water-Equivalent-Hydrogen > 26 %[44]. Dark red line, outline of lower member of MFF. Green line, aligned knobs[45,46]. Black arrows, Aeolis Mensae outcrops within the MFF. Yellow triangle, Curiosity rover location. Basemap, stretched MOLA elevation over MOLA Hillshade.

Methods

Computation of synthetic spectra and CH_4 retrieval algorithm.

We developed an algorithm to retrieve methane abundance (volume mixing ratio, vmr) on Mars from the PFS SWC spectra. The algorithm includes a radiative transfer (RT) code developed for the analysis of PFS SWC spectra with a full treatment of the multiple scattering (MS) problem. The retrieval algorithm relies on the Levenberg-Marquardt approach[51,52].

The computation of synthetic spectra relies on the DISORT (Discrete Ordinates Radiative Transfer Program for a Multi-Layered Plane-Parallel Medium) solver implemented in the ARS code[53] and specifically developed for the analysis of PFS spectra. DISORT is a general and versatile plane-parallel radiative transfer program applicable to problems from the ultraviolet to the radar regions of the electromagnetic spectrum[54], which includes a full treatment of atmospheric multiple scattering by suspended particles. The synthetic spectra are obtained performing the line-by-line computation and then filtering the result with the newly retrieved PFS apodized instrumental line shape (ILS) described above. We use HITRAN 2012[55] as spectroscopic database. The absorption coefficients $k(\nu,p,T)$ at the i-th atmospheric layer [cm^{-1}] are defined as:

$$k_i(\nu,p,T) = ACS_i(\nu,p_i,T_i) \cdot n_i$$

where ν is the wavenumber [cm^{-1}], p_i and T_i are the pressure [mbar] and the temperature [K] at the i-th layer, respectively. ACS_i is the absorption cross section calculated from HITRAN 2012 using a Voigt profile [cm^{-1}/(molecule × cm^{-2})/cm^{-1}] and n_i is the number density [cm^{-3}] calculated from the pressure and temperature using the perfect gas law. The absorption coefficients are calculated using a line-by-line approach[54].

The use of an appropriate solar spectrum is also important for analysis of infrared spectra, in particular with relatively high spectral resolution, because Fraunhofer lines mix up with H_2O absorption features in the considered spectral range. The PFS team has made a significant effort to construct a high-resolution Solar spectrum[56] used in this analysis. The commonly used spectrum[57] has disadvantages, being either purely theoretical within the H_2O bands, and undersampled for our purpose (1-cm^{-1} bins).

In order to calculate the synthetic spectra, a series of parameters that describe the atmospheric layers at the time of the observations must be specified as input parameters to the RT code. The initial guess for the H_2O abundance (vertical profile) and the surface pressure are the only parameters extracted from the General Circulation Model (EMCD v5.2[58,59]), at the time (Solar Longitude L_s, and Local Time LT) and location (latitude and longitude) of the PFS measurements. For the surface pressure we make use of pres0, a routine to estimate surface pressure with high accuracy, using high resolution (32pix/deg.) MOLA topography, provided with EMCD 5.2. The initial abundance of methane is set to 0 ppbv. All the other relevant atmospheric, namely the atmospheric temperature profile as a function of pressure and altitude, the surface temperature, and the integrated dust and water ice opacity, are retrieved[60,61] from the PFS LWC measurements acquired simultaneously to those of the SWC used for the CH_4 retrievals.

In order to retrieve methane abundance, the synthetic spectra calculated as described above, are best-fitted to the PFS average spectra. The retrieval algorithm relies on the minimization of the sum of the squares of the differences between the measured radiances and a parameterized function (least squares problem). To solve the nonlinear least squares problem, we adopted the Levenberg-Marquardt approach[51,52].

To retrieve methane mixing ratio we use PFS SWC average spectra in the reduced spectral range 3001 – 3031 cm^{-1}, which includes several absorption bands of water vapor, a Solar band, and the CH_4 Q-branch at 3018 cm^{-1} (e.g., **Figs. S2, S5 and S6**). Three parameters are considered in the iterative retrieval: the surface albedo, the water abundance, and the methane mixing ratio. The goodness of fit between radiance measurements and synthetic spectra is checked at each iteration by using chi-squared error criterion $\chi^2(a)$. The improvements Δa of a retrieved parameter a are performed by using the non-dimensional scalar factor λ presented in the formula:

$$[J^T WJ+ \lambda\cdot \mathrm{diag}(J^T WJ)]\cdot\Delta a = J^T W(y - y') \qquad \text{(Eq. 1)}$$

where:

J – Jacobian matrix, derivative of fitted function with respect to each parameter;

W – inverse of the measurement error covariance matrix;

y – measured spectrum;

y' – synthetic spectrum.

The steps required and implemented in our algorithm for the Levenberg-Marquardt approach[62] can be summarized as follows:

1) Calculate the $\chi^2(a)$ using a first-guess of the parameters a to be retrieved;
2) Δa is calculated by **Eq. 1** assuming an initial modest value for λ in the first iteration: $\lambda = \lambda_0$;
3) calculate the synthetic spectrum with updated parameters $a + \Delta a$;
4) evaluation of $\chi^2(a + \Delta a)$;
5) update value of λ:
    a. if $\chi^2(a + \Delta a) \geq \chi^2(a)$, increase λ by a “substantial” factor f_+: $\lambda_{i+1} = \lambda_i \cdot f_+$, ($i$ is the iteration number);
    b. if $\chi^2(a + \Delta a) < \chi^2(a)$, decrease λ by a “substantial” factor f_-: $\lambda_{i+1} = \lambda_i / f_-$;
6) repeat steps 3) to 5) until final solution is approached;
7) the algorithm is stopped when the convergence criterion is reached.

The Levenberg-Marquardt parameters λ_0, f_+, and f_- have been estimated from preliminary tests on the retrieval algorithm by assuming a wide range of possible values and by the comparison of $\chi^2(a)$ and $\chi^2(a + \Delta a)$ in the various iterations. A good compromise between accuracy of retrieval (minimization of $\chi^2(a)$), number of iteration required to reach the convergence criterion, and the required computational time is found for the following values of the above parameters, which have been adopted in the final implementation of the algorithm: $\lambda_0=10^{-2}$; $f_+=10^5$ and $f_- = 10$.

Also necessary is a condition for stopping. Iterating to convergence (to machine accuracy or to the round-off limit) is generally wasteful and unnecessary since the minimum is at best only a statistical estimate of the parameters (a). A change in the parameters that changes χ^2 by an amount << 1 is never statistically meaningful[61]. In practice, it is recommended to stop iterating on the first or second occasion that decreases by a negligible amount, being either less than 0.01 absolutely or, in case round-off prevents that being reached, some fractional amount like 10^{-3} [62]. It is also recommended to avoid a stop after a step where χ^2 increases: that only shows that it has not yet adjusted itself optimally[61]. In our case, as a convergence criterion we stop iterating when the following conditions are satisfied: $\chi^2(a + \Delta a) - \chi^2(a) < 0$ and $|\chi^2(a + \Delta a) - \chi^2(a)| < \chi^2(a + \Delta a) \cdot 10^{-3}$.

We applied the retrieval algorithm described above to the PFS spot-tracking observations over Gale crater listed in **Table S1** as well as to the standard nadir observations listed in **Table 1**. Only dayside observations with > 200 measurements were considered. Methane is only detected in orbit 12025, where PFS collected 280 measurements in about 45 minutes in spot-tracking mode. The results are shown in **Fig. 1**. The actual footprints of PFS observations and the retrieved atmospheric temperature profiles used as input for the computation of synthetic spectra are shown in **Fig. S9a,b**.

GCM simulations.

The GEM-Mars three-dimensional general circulation model (GCM) for the atmosphere of Mars[40] applied in this work was operated at a 4°×4° horizontal resolution and with 103 vertical levels extending from the surface to ~7×10^{-6} Pa (~140 km). The vertical resolution in the lowermost atmosphere is fine: the spacing between levels is ~15 m near the surface and ~1 km at 10 km in height. The model time step is 1/48 of a sol (~30 minutes). The model was extensively validated against multiple datasets[40], and was previously applied for the study of fine dust layers observed by the Phoenix Mars mission[41], for the simulation of the annual cycles of water vapour and carbon monoxide on Mars[63], for the simulation of the Mars dust cycle[64], and for the transport of methane upon surface release[28]. GEM-Mars forms an integral part in the analysis and interpretation of data from the NOMAD spectrometer on the ESA-Roskosmos ExoMars Trace Gas Orbiter[47,65,66,67].

The accuracy of the simulated wind fields can be optimized by constraining the dynamical model fields by available observations. To do this, the atmospheric dust content in the GCM was imposed to be in accordance with the dust observations by the PFS obtained during MEx orbits 12018 (nadir) and 12025 (spot-tracking) (**Table 1** and **Fig. S9c**). GEM-Mars has an active dust lifting scheme but the simulated dust optical depth (OD) was scaled at all times to the climatological values for Martian year 31[68], binned over 10° L_s. In the region of Gale crater, the climatological value for L_s=330°–340° (OD=0.62) was considerably larger than that measured by PFS (average OD ~0.30). The model dust OD was scaled globally in this time window by the ratio 0.30/0.62 to ensure that the dust OD in the Gale crater area matches the PFS value at the time of the observations (**Fig. S9c**). It was verified that the simulated temperature profile at the time of the PFS observation matched with the PFS retrieved temperature profile during orbit 12025 (**Fig. S9b**). The model temperature profile shown in **Fig. S9b** is an average of 70 profiles that are randomly distributed within the PFS orbit 12025 footprint (**Fig. S9a**) at 9:40 LTST on sol 306. These model profiles were interpolated from the model grid and corrected for pressure taking into account the height difference between the coarse-grained model grid and the high-resolution MOLA topography.

For each of the 30 grid cells considered as emission sites, a simulation was performed involving the release of 120 tracers (see below). The simulations were fully parallelized on 24 nodes of BIRA-IASB's High-Performance cluster.

Statistical approach.

The statistical approach adopted here, belonging to the Monte-Carlo-type approaches, is based on the assumption that the inert tracers (such as methane, on the considered timescales) simulated in a GCM are linearly additive. This was explicitly verified by test simulations (relative error of ~0.05%). As a corollary, they can also be scaled by any factor. In addition, while the model time step is ~30 minutes, the average of two tracers released at an interval of one hour describes fairly well the evolution of the tracer released in between (relative error of ~3%). In practice, in this model study, 120 tracers were released successively every hour from any model grid cell. Exploiting the last assumption, the tracers released at the 119 model time steps in between can be reasonably considered as the average of tracers on both sides, so raising to 239 the total number of available tracers.

Let $N = 239$ and $M_r = 10^5$ kg be respectively the number of tracers and the initial mass of each tracer T_i released at time t_i. If the mass of tracer T_i is scaled by a factor $\varphi_i(t_i)$ arbitrarily chosen, the mass M_{0i} of T_i released into the atmosphere becomes: $M_{0i} = \varphi_i(t_i)M_r$.

In order to match the first and last observational constraints (**Table 1**), it was verified from test simulations that the event started at the earliest at midnight on sol 302, and lasted no longer than until the end of sol 306. On the other hand, the event started necessarily prior to sol 305 at 13h, i.e. at the time of the methane detection by Curiosity. Finally, the minimum emission duration is 30

Mars minutes (i.e. one model time step). Thus, being t_0 the initial time and τ the duration of the event, we have

$$0\ \text{h} \leq t_0 \leq 85\ \text{h}\ \ (\text{i.e. between sol 302 at 0 h and sol 305 at 13 h})$$

$$\tau_{\min} \leq \tau \leq \tau_{\max} \quad \text{where} \quad \begin{cases} \tau_{\min} = 30\ \text{minutes} \\ \tau_{\max} = 5\ \text{sols} \end{cases}$$

where $\tau_{\min}$ and $\tau_{\max}$ are the minimum and maximum durations, respectively. As a result, depending on t_0 and τ, $T_i(t_i)$ is zeroed if its emission time t_i is outside the time period of the event. These conditions can be rewritten in terms of Heaviside step functions as

$$\theta_1(t_i - t_0) = \begin{cases} 1\,, & t_i \geq t_0 \\ 0\,, & t_i < t_0 \end{cases}$$

$$\theta_2(t_0 + \tau - t_i) = \begin{cases} 1\,, & t_i \leq t_0 + \tau \\ 0\,, & t_i > t_0 + \tau \end{cases}$$

and the effective mass M_{0i} of T_i released at time t_i takes the form

$$M_{0i} = \varphi_i(t_i, t_0, \tau) M_r = \varphi_i(t_i)\,\theta_1(t_i - t_0)\,\theta_2(t_0 + \tau - t_i)\,M_r = \begin{cases} \varphi_i(t_i) M_r\,, & t_0 \leq t_i \leq t_0 + \tau \\ 0\,, & t_i < t_0 \text{ or } t_i > t_0 + \tau \end{cases}$$

The total mass M_0 of tracers released during the event occurring between t_0 and $t_0 + \tau$ is thus given by

$$M_0 = \sum_{i=1}^{N} \varphi_i(t_i, t_0, \tau) M_r$$

For the sake of conciseness, Greek and Latin letters will indicate the measurements (retrieved abundance of methane) and the corresponding model variables (mean abundance for the same area and temporal interval of the observations), respectively. Let $\{\alpha,\beta,\gamma,\delta,\varepsilon,\zeta\}$ be the set of observational constraints reported in **Table 1**:

$$\text{MSL (sol 305)}: \alpha \pm \Delta\alpha = 5.78 \pm 2.27 \text{ ppbv}$$
$$\text{PFS (sol 306)}: \beta \pm \Delta\beta = 15.5 \pm 2.5 \text{ ppbv}$$
$$\text{MSL (sol 313)}: \gamma \pm \Delta\gamma = 2.13 \pm 2.02 \text{ ppbv}$$
$$\text{PFS (sol 304)}: \delta = 3 \text{ ppbv}$$
$$\text{PFS (sol 316)}: \varepsilon = 5 \text{ ppbv}$$
$$\text{PFS (sol 318)}: \zeta = 5 \text{ ppbv}$$

Let {A, B, C, D, E, F} be the set of model variables that must fit the observational dataset $\{\alpha,\beta,\gamma,\delta,\varepsilon,\zeta\}$. A release scenario is said consistent with the observations if and only if the following relations are satisfied:

$$\begin{cases} \alpha - \Delta\alpha \le A \le \alpha + \Delta\alpha \\ \beta - \Delta\beta \le B \le \beta + \Delta\beta \\ \gamma - \Delta\gamma \le C \le \gamma + \Delta\gamma \\ 0 \le D \le \delta \\ 0 \le E \le \varepsilon \\ 0 \le F \le \zeta \end{cases}$$

Let $\{A_{0i}, B_{0i}, C_{0i}, D_{0i}, E_{0i}, F_{0i}\}$ be the set of model variables that result from the emission of the initial mass M_r of the single tracer T_i. Those variables are obtained by linear interpolation at the time and location of the corresponding observations. As they depend linearly on M_{0i}, they are scaled by the same factor $\varphi_i(t_i, t_0, \tau)$. Consequently, the model variables $\{A_0, B_0, C_0, D_0, E_0, F_0\}$ can be written as

$$\begin{cases} A_0 = \sum_{i=1}^{N} \varphi_i(t_i, t_0, \tau) A_{0i} \\ B_0 = \sum_{i=1}^{N} \varphi_i(t_i, t_0, \tau) B_{0i} \\ \vdots \\ F_0 = \sum_{i=1}^{N} \varphi_i(t_i, t_0, \tau) F_{0i} \end{cases}$$

We generate 10^6 potential release events for each of the 30 emission sites considered by generating the same amount of random combinations of the parameters φ_i, t_0, τ. Then, for each single event, the model variables can be scaled by a factor f in order to match the observations, when possible. This factor must satisfy six constraining relations in terms of the six observations:

$$\begin{cases} \frac{\alpha - \Delta\alpha}{A_0} \leq f_A \leq \frac{\alpha + \Delta\alpha}{A_0} \\ \frac{\beta - \Delta\beta}{B_0} \leq f_B \leq \frac{\beta + \Delta\beta}{B_0} \\ \frac{\gamma - \Delta\gamma}{C_0} \leq f_C \leq \frac{\gamma + \Delta\gamma}{C_0} \\ 0 \leq f_D \leq \frac{\delta}{D} \\ 0 \leq f_E \leq \frac{\varepsilon}{E} \\ 0 \leq f_F \leq \frac{\zeta}{F} \end{cases}$$

or, more simply:

$$\boldsymbol{f}_{\min} \leq \boldsymbol{f} \leq \boldsymbol{f}_{\max}$$

where $\boldsymbol{f} = \{f_A, f_B, f_C, f_D, f_E, f_F\}$.

A scenario is said to be consistent with the observations if it exists f such that:

$$\max(\boldsymbol{f}_{\min}) \le f \le \min(\boldsymbol{f}_{\max})$$

If so, f is arbitrarily chosen as the mean value between $\max(\boldsymbol{f}_{\min})$ and $\min(\boldsymbol{f}_{\max})$:

$$f = \frac{\max(\boldsymbol{f}_{\min}) + \min(\boldsymbol{f}_{\max})}{2}$$

As described above, a sequence of stochastic fluxes is generated to produce a release pattern that mimics an episodic seepage event. In practice, this procedure consists in generating ***randomly*** factors $\{\varphi_i(t_i)\}$ given by a probability distribution function. $\varphi_i(t_i)$ was defined as the factor scaling the initial mass M_r of tracer T_i, so that

$$\varphi_i(t_i) = \frac{M_{0i}}{M_r}$$

If a mass M_{0i} is released from a surface area S during one model time step Δt, the resulting release rate $\chi_{0i}(t_i)$ of T_i is given by:

$$\chi_{0i}(t_i) = \frac{M_{0i}}{S\Delta t}$$

Therefore, $\varphi_i(t_i)$ takes the form

$$\varphi_i(t_i) = \frac{S\Delta t}{M_r}\chi_{0i}(t_i)$$

Let $P(\chi)$ be a probability distribution function of the release rate χ used to generate randomly a release pattern. Given that the time evolution of gas fluxes is not known even on Earth, we chose the simplest function, i.e. the uniform distribution function:

$$P_u(\chi) = \frac{1}{X_0}; \quad 0 \leq \chi \leq X_0$$

where X_0 was fixed to 150 mg m^{-2} day^{-1}. This value is arbitrary but does not affect the final results because the tracers are all scaled by a factor f afterwards. Any other distribution function could be used. In our study, in order to test the sensitivity of the analysis to the variability of gas fluxes and to estimate the robustness of the statistical results, we also considered a Gaussian distribution function:

$$P_G(\chi) = \frac{1}{\sqrt{2\pi\sigma^2}} \exp\left(-\frac{(\chi-\mu)^2}{2\sigma^2}\right); \quad 0 \leq \chi \leq \infty$$

where μ = 75 mg m^{-2} day^{-1} and σ = 20 mg m^{-2} day^{-1}. The good agreement between the so-obtained probability map (not shown) and that displayed in **Fig. 3** indicates that the probabilities of fitting the observations do not depend dramatically on the gas flux variability, which emphasizes the robustness of our results.

Finally, the initial time t_0 and duration τ of the release event are generated randomly using a uniform distribution function.

An example scenario is presented in **Figs. S13-S15**. **Fig. S13** illustrates the procedure followed to produce one release pattern. **Fig. S14** shows the time evolution of the simulated methane abundance at Gale crater and the procedure to scale the tracers in order to match the observations. **Fig. S15** finally shows maps of the simulated methane abundance for the times of the available observations.

Geological analysis.

For the GCM simulations, we considered terrestrially realistic methane emission patterns (i.e., release intensity, duration, variation and area), based on gas seepage theory and experimental data acquired on Earth (e.g., ref. [42] and references therein). For definition and description of the various "seepage" terms used here, the reader may refer to refs [42, 69-76]. Details are provided in SI-2.

For Martian geological context, we analysed image data from the Mars Orbiter Laser Altimeter (MOLA) on Mars Global Surveyor as well as the Context camera (CTX) and High Resolution Imaging Science Experiment (HiRISE) on Mars Reconnaissance Orbiter, incorporating information from published geological maps and reports. We initially evaluated a wide area, ~1000-km-radius, surrounding Gale crater. However, GCM simulations indicated that features more than ~800 km from Gale would be unlikely to account for the Gale detections. Emphasis was then placed on the grid areas used in the GCM simulations. All data were mapped using Esri's ArcGIS software and the U.S. Geological Survey Mars Global GIS v2.1 (outline of the Medusae Fossae Formation from geological global map I-1802ABC). Details are provided in SI-2.

Data availability

The PFS data used in this study are publicly available via the ESA Planetary Science Archive. References of terrestrial gas seepage data are reported in the SI. Data used to map water-equivalent-hydrogen are available from Jack T. Wilson (Durham University, UK). All other geological data of Mars used in this study are in the public domain and include published papers, data provided in the U.S. Geological Survey MarsGlobal GIS v2.1 (which can be accessed on their Mars GIS FTP site - file name: MarsGIS_Equi0_v21.zip [note: v21 used in the file name for v2.1]), and CTX and Visible data image mosaics provided by Google Earth (Mars).

Code availability

The core GEM model used for this work is publicly available through http://collaboration.cmc.ec.gc.ca/science/rpn.comm/. The routines that were modified for the application to Mars were explained in *ref.*[40] and are available upon request from authors L.N., F. D. and S. V. The model output used in this paper is available by request from authors S.V., F.D. and L.N. The equations for the statistical analysis are included in Methods. The computer code to reproduce them is available from author S.V.

References only in Methods

51. Levenberg, K., A Method for the Solution of Certain Non-Linear Problems in Least Squares. The Quarterly of Applied Mathematics 2, 164–168 (1944). doi:10.1090/qam/10666

52. Marquardt, D.W., An algorithm for least-squares estimation of nonlinear parameters, *Journal of the Society for Industrial and Applied Mathematics* **11**(2), 431–441 (1963).

53. Ignatiev, N. I., Grassi, D. & Zasova, L. V., Planetary Fourier spectrometer data analysis: fast radiative transfer models. *Planet. Space Sci.* **53**, 1035–1042 (2005).

54. Stamnes, K., Tsay, S. C., Wiscombe, W. & Jayaweera, K., Numerically stable algorithm for discrete-ordinate-method radiative transfer in multiple scattering and emitting layered media, *Appl. Opt.* **27** (12), 2502–2509 (1988).

55. Rothman, L. S et al., The HITRAN2012 molecular spectroscopic database, *J. Quant. Spectrosc. Radiat. Transf.* **130**, 4–50 (2013).

56. Fiorenza, C. & Formisano, V., A solar spectrum for PFS data analysis, *Planet. Space Sci.* **53**, 1009–1016 (2004).

57. Kurucz, R., *The solar spectrum: atlases and line identifications. In Laboratory and Astronomical High Resolution Spectra*, Astron. Soc. of the Pacific Conf. Series 81, (eds. A.J. Sauval, R. Blomme, and N. Grevesse) 17–31 (1995).

58. Millour, E., et al., The Mars Climate Database (MCD version 5.2). European Planetary Science Congress 2015, held 27 September – 2 October, 2015 in Nantes, France (2015). Abstract 10:EPSC2015-438.

59. Forget, F., et al., Improved general circulation models of the Martian atmosphere from the surface to above 80 km, *J. Geophys. Res.* **104** (E10), 24155–24176 (1999).

60. Grassi D., et al., Methods for the analysis of data from the Planetary Fourier Spectrometer on the Mars Express Mission. *Planet. Space Sci.* **53**, 1017–1034 (2005). doi:10.1016/j.pss.2005.01.006.

61. Wolkenberg, P., et al., Characterization of dust activity on Mars from MY27 to MY32 by PFS-MEX observations; *Icarus* **310**, 32–47 (2018). doi:10.1016/j.icarus.2017.10.045

62. Press W. H., Teukolsky, S. A., Vetterling, W. T. & Flannery, B. T., *Numerical Recipes* 3rd Edition: The Art of Scientific Computing, Cambridge University Press, New York, NY (2007).

63. Smith, M., Daerden, F., Neary, L. & Khayat, S., The climatology of carbon monoxide and water vapor on Mars as observed by CRISM and modeled by the GEM-Mars general circulation model. Icarus, 301, 117–131 (2018). doi:10.1016/j.icarus.2017.09.027

64. Musiolik, G., et al., Saltation under Martian Gravity and its Influence on the Global Dust Distribution. *Icarus* **306**, 25–31 (2018). doi:10.1016/j.icarus.2018.01.007.

65. Vandaele, A.C., et al., Science objectives and performances of NOMAD, a spectrometer suite for the ExoMars TGO mission. *Planet. Sp. Sci.* **119**, 233-249 (2015). doi:10.1016/j.pss.2015.10.003

66. Robert, S., et al., Expected performances of the NOMAD/ExoMars instrument. *Planet. Sp. Sci.* **124**, 94–104 (2016). doi:10.1016/j.pss.2016.03.003

67. Robert, S., et al., Two test-cases for synergistic detections in the Martian atmosphere: Carbon monoxide and methane. *J. Quant. Spectrosc. Radiat. Transf.* **189**, 86–104 (2017), doi:10.1016/j.jqsrt.2016.11.003.

68. Montabone, L., et al., Eight-year climatology of dust optical depth on Mars. *Icarus* **251**, 65–95 (2015), doi:10.1016/j.icarus.2014.12.034.

69. Abrams, M.A., Significance of hydrocarbon seepage relative to petroleum generation and entrapment. *Mar. Pet. Geol.* **22**, 457–477 (2005).

70. Etiope G. & Klusman R.W., Microseepage in drylands: flux and implications in the global atmospheric source/sink budget of methane. *Global Planet. Change* **72**, 265–274 (2010).

71. Etiope, G., Nakada, R., Tanaka, K., & Yoshida, N., Gas seepage from Tokamachi mud volcanoes, onshore Niigata basin (Japan): origin, post-genetic alterations and CH_4-CO_2 fluxes. *Appl. Geochem.* **26**, 348–359 (2011).

72. Klusman, R.W., Leopold, M.E. & LeRoy, M.P., Seasonal variation in methane fluxes from sedimentary basins to the atmosphere: results from chamber measurements and modeling of transport from deep sources. *J. Geophys. Res.: Atm.* **105**, 24661–24670 (2000)

73. Macgregor, D.S., Relationships between seepage, tectonics and subsurface petroleum reserves. *Mar. Pet. Geol.* **10**, 606–619 (1993).

74. Malmqvist, L. & Kristiansson, K., A physical mechanism for the release of free gases in the lithosphere. *Geoexploration* **23**, 447–453 (1985).

75. Mazzini, A. & Etiope, G., Mud volcanism: an updated review. *Earth-Sci. Rev.* **168**, 81–112 (2017).

76. Schumacher, D., Hydrocarbon-induced alteration of soils and sediments, hydrocarbon migration and its near-surface expression. In *Hydrocarbon Migration and Its Near-Surface Expression*, AAPG Memoir 66, edited by D. Schumacher and M.A. Abrams, PennWell Publishing, Tulsa, OK, pp 71–89 (1996).

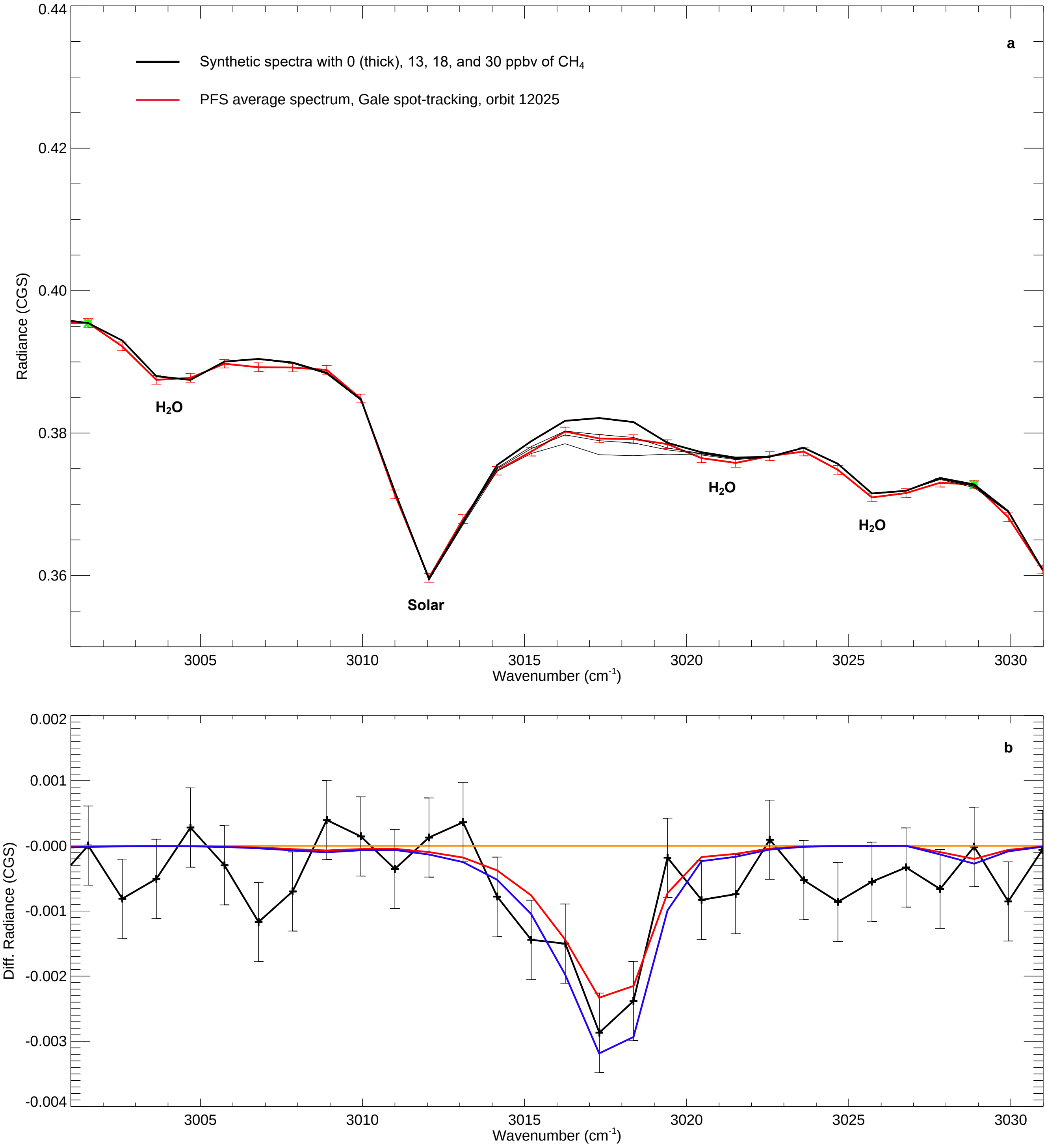

a
Synthetic spectra with 0 (thick), 13, 18, and 30 ppbv of CH_4
PFS average spectrum, Gale spot-tracking, orbit 12025
H_2O
Solar
H_2O
H_2O
Radiance (CGS)
0.44
0.42
0.40
0.38
0.36
Wavenumber (cm^{-1})
3005
3010
3015
3020
3025
3030
b
Diff. Radiance (CGS)
0.002
0.001
-0.000
-0.001
-0.002
-0.003
-0.004
Wavenumber (cm^{-1})
3005
3010
3015
3020
3025
3030

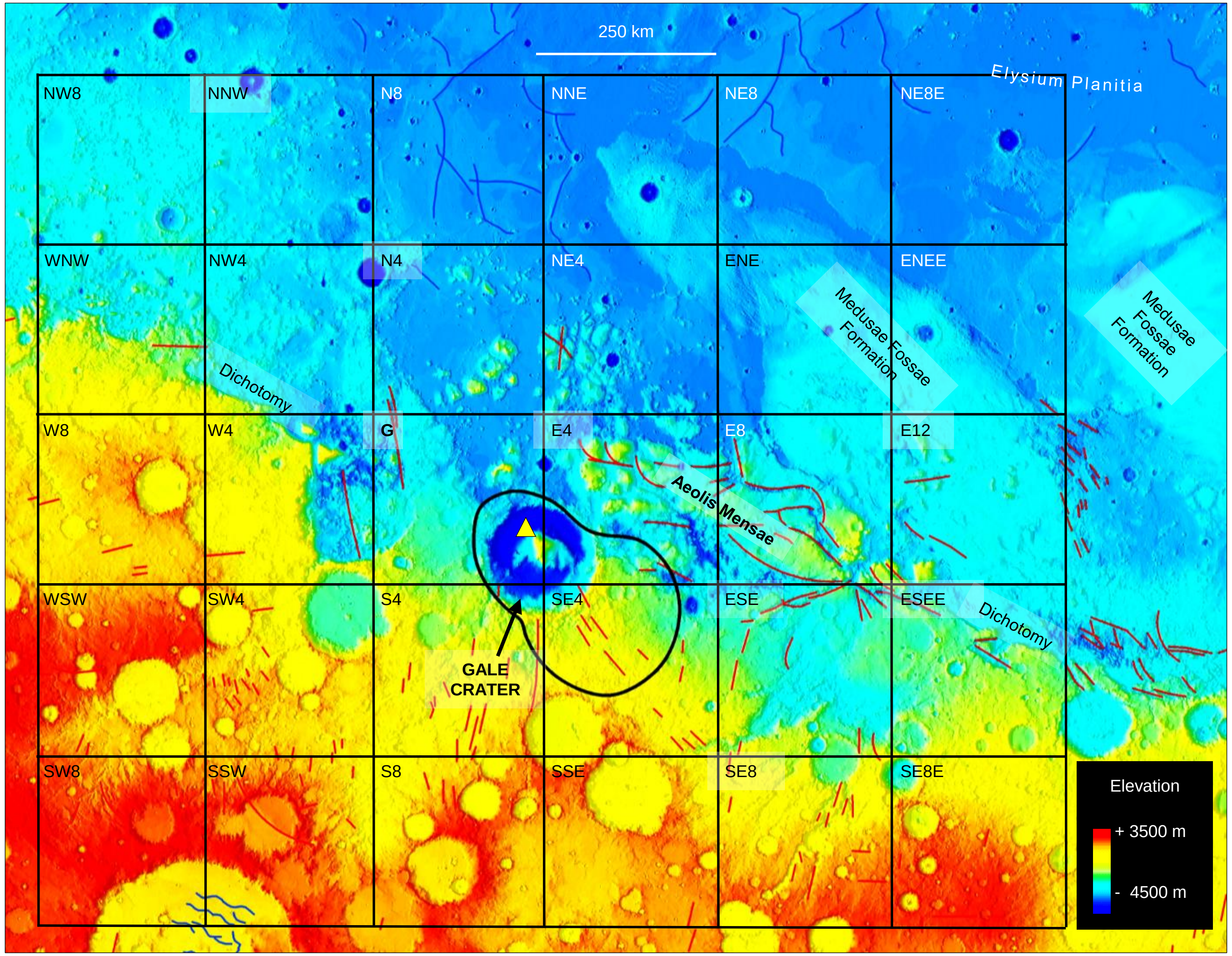
250 km
Elysium Planitia
NW8
NNW
N8
NNE
NE8
NE8E
WNW
NW4
N4
NE4
ENE
ENEE
Medusae Fossae Formation
Medusae Fossae Formation
Dichotomy
W8
W4
G
E4
E8
E12
Aeolis Mensae
WSW
SW4
S4
SE4
ESE
ESEE
Dichotomy
GALE CRATER
SW8
SSW
S8
SSE
SE8
SE8E
Elevation
+ 3500 m
- 4500 m

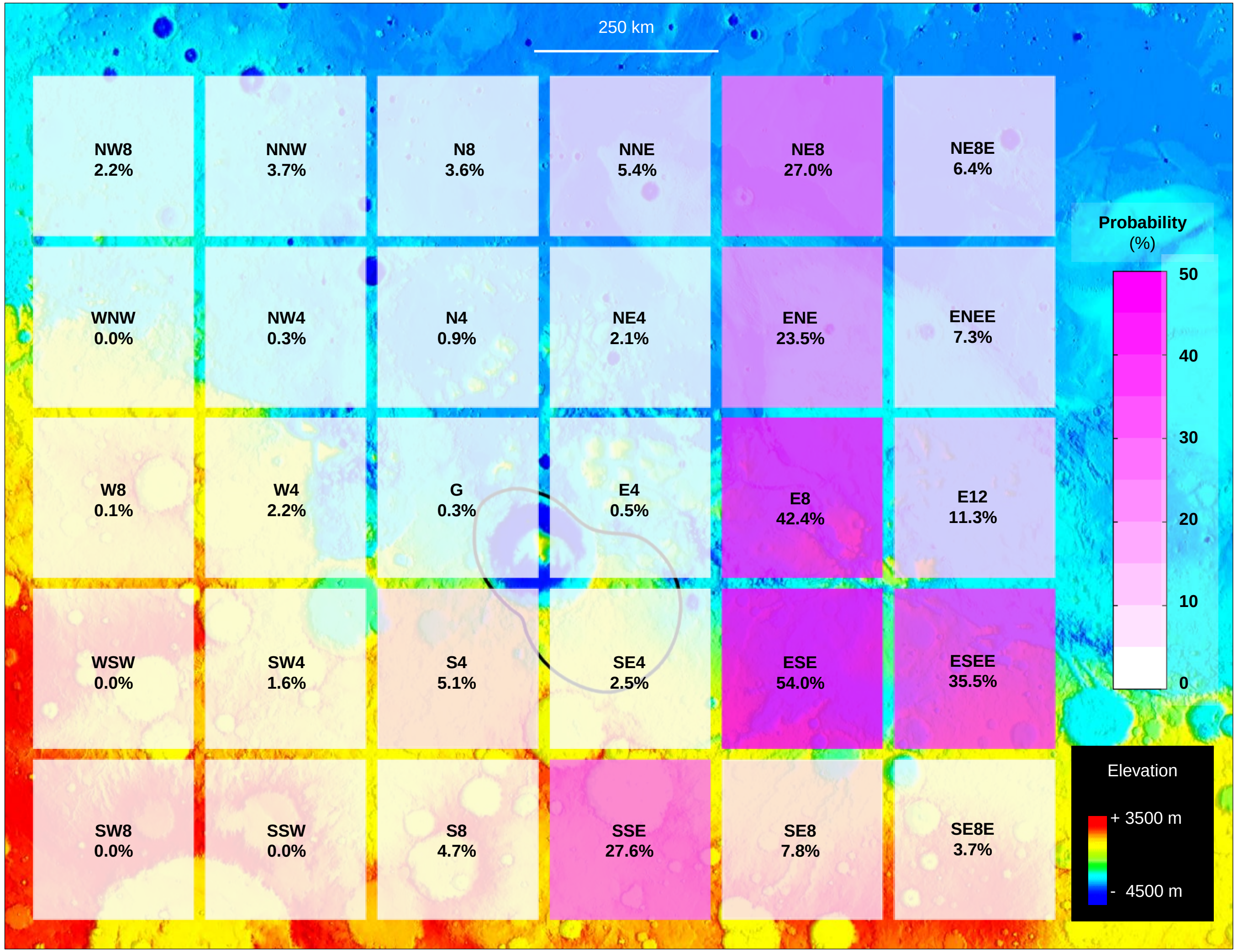

250 km
NW8
2.2%
NNW
3.7%
N8
3.6%
NNE
5.4%
NE8
27.0%
NE8E
6.4%
WNW
0.0%
NW4
0.3%
N4
0.9%
NE4
2.1%
ENE
23.5%
ENEE
7.3%
W8
0.1%
W4
2.2%
G
0.3%
E4
0.5%
E8
42.4%
E12
11.3%
WSW
0.0%
SW4
1.6%
S4
5.1%
SE4
2.5%
ESE
54.0%
ESEE
35.5%
SW8
0.0%
SSW
0.0%
S8
4.7%
SSE
27.6%
SE8
7.8%
SE8E
3.7%
Probability
(%)
50
40
30
20
10
0
Elevation
+ 3500 m
- 4500 m

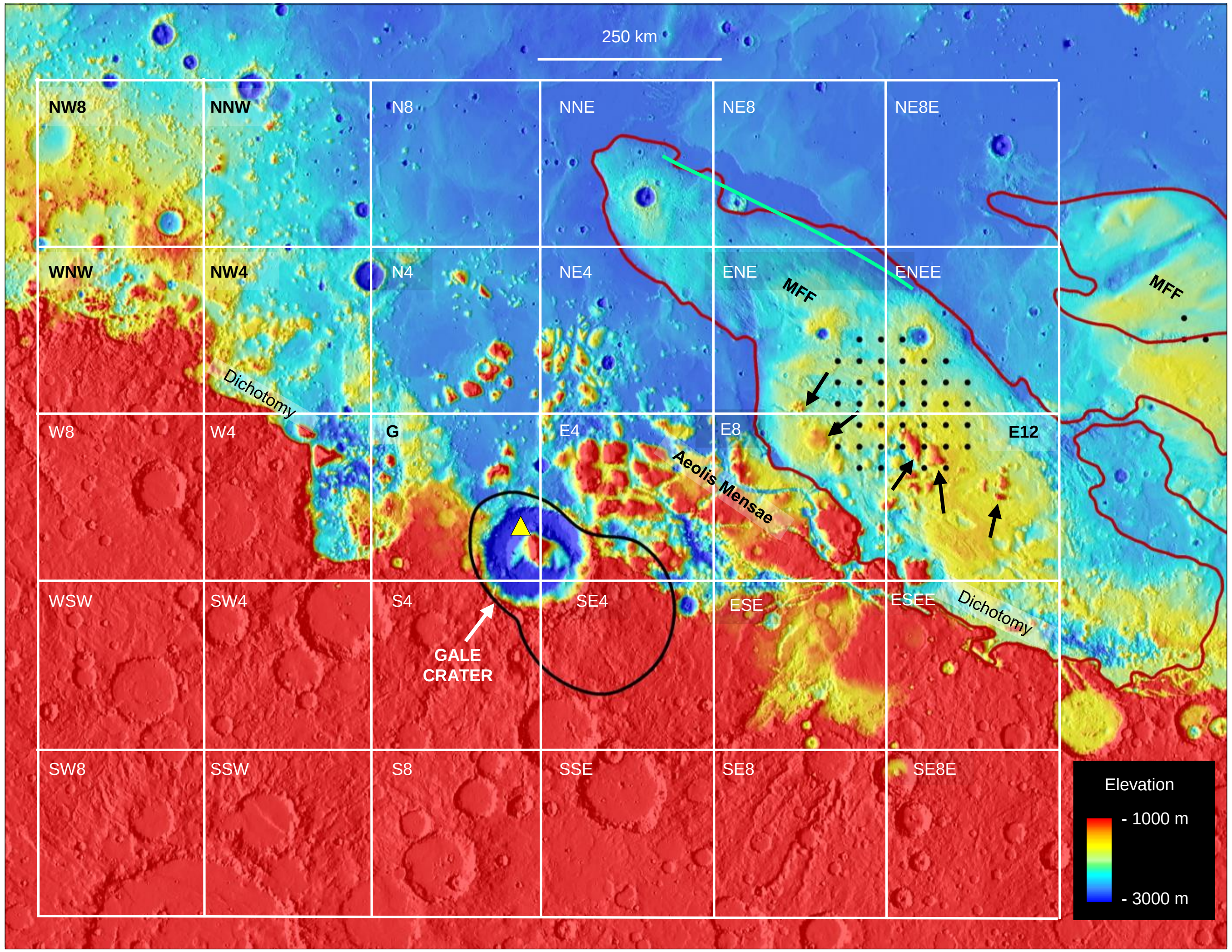

250 km
NW8
NNW
N8
NNE
NE8
NE8E
WNW
NW4
N4
NE4
ENE
ENEE
MFF
MFF
Dichotomy
W8
W4
G
E4
E8
E12
Aeolis Mensae
WSW
SW4
S4
SE4
ESE
ESEE
Dichotomy
GALE
CRATER
SW8
SSW
S8
SSE
SE8
SE8E
Elevation
- 1000 m
- 3000 m

Table 1. **List of observational constraints.** The first column provides the number of sols before (negative values) or after the TLS-SAM measurements on sol 305. The positive detections are in bold. Upper limits are provided (1-σ uncertainty) when no CH_4 band is observed in PFS spectra.

Sols	Date[a]	Time	MEx Orbit[e]	Value (ppbv)	Instrument
-1	Sol 304	~9:45[b] (LTST[d])	12018	≤ 3 ppbv	PFS
0	**Sol 305**	**13:00[c] (LTST)** **ingestion: 20'**	**N/A**	**5.78 ± 2.27**	**TLS-SAM**
1	**Sol 306**	**9:41[c] (LTST):** **meas. duration: 43'**	**12025[f]**	**15.5 ± 2.5**	**PFS**
8	**Sol 313**	**N/A**	**N/A**	**2.13 ± 2.02**	**TLS-SAM**
11	Sol 316	~9:24[b] (LTST)	12060	≤ 5	PFS
13	Sol 318	~9:19[b] (LTST)	12067	≤ 5	PFS

[a] Sols since MSL landing, Sol 305 = June 15, 2013. [b] Average time of orbit. [c] Starting time of observation. [d] Local True Solar Time. [e] Orbit tracks and PFS footprints are shown in **Fig. S12a**. [f] Spot-tracking observation.